Phonon signatures for polaron formation in an anharmonic semiconductor

Journal Article

Author(s):
Wang, Feifan (iD); Chu, Weibin; Huber, Lucas; Tu, Teng; Dai, Yanan; Wang, Jue; Peng, Hailin; Zhao, Jin; Zhu, Xiaoyang

Supplementary Information

Phonon Signatures for Polaron Formation in an Anharmonic Semiconductor

Feifan Wang[1,#],Weibin Chu[2,3,#], Lucas Huber[1], Teng Tu[4], Yanan Dai[1], Jue Wang[1], Hailin Peng[4], Jin Zhao[2,5,*], Xiaoyang Zhu[1,*]

[1]Department of Chemistry, Columbia University, New York, NY10027, USA

[2]ICQD/Hefei National Laboratory for Physical Sciences at Microscale, CAS Key Laboratory of Strongly-Coupled Quantum Matter Physics, and Department of Physics, University of Science and Technology of China, Hefei, Anhui 230026, China.

[3]Departments of Chemistry, University of Southern California, Los Angeles, CA 90089, USA States.

[4]Center for Nanochemistry, Beijing Science and Engineering Center for Nanocarbons, Beijing National Laboratory for Molecular Sciences, College of Chemistry and Molecular Engineering, Peking University, Beijing 100871, China.

[5]Synergetic Innovation Center of Quantum Information & Quantum Physics, University of Science and Technology of China, Hefei, Anhui 230026, China.

[*]Corresponding authors. xyzhu@columbia.edu (XYZ); zhaojin@ustc.edu.cn (JZ)

[#]These authors contributed equally to this work.

Materials and Methods.

Single crystal growth. Bi_2O_2Se bulk crystals are synthesized by a modified Bridgman method via two steps. Frist, stoichiometric high-purity Bi_2O_3 powder (Alfa Aesar, 5 N) and Bi_2Se_3 pieces (Alfa Aesar, 5 N) are ground into fine powders and well mixed. The mixed powders are placed in a quartz tube which is vacuumized and sealed with pressure down to 10^{-2} Pa. The high-purity Bi_2O_2Se powder is obtained by keeping the raw materials reacting at 1123 K over 48 h. Second, Bi_2O_2Se powder is ground and placed in an evacuated quartz tube for crystallization. A melting temperature is needed for this process. By keeping the Bi_2O_2Se powder at melting temperature of 1223 K for 5 min and slowly cooling to 1163 K over 9 h, the Bi_2O_2Se crystal with size of 5~9 mm is finally obtained.

Coherent phonon spectroscopy. The fundamental pulse (1.55 eV, 0.8 mJ/pulse, pulse duration ~ 35 fs) from a 10 kHz Ti:sapphire regenerative amplifier (Legend, Coherent Inc.) was split into pump and probe lines. The different-color pump pulses were generated from a homebuilt noncolinear optical parametric amplifier (NOPA) and the corresponding pulse durations were measured by the frequency-resolved optical grating (FROG) method (detailed in Fig. S10). The probe pulse was delivered by the attenuated fundamental at pulse energy < 500 nJ. The pump spot size of ~160 µm on the sample was set to be much larger than the probe spot (30 µm) to ensure homogeneous excitation. A balanced detection scheme was used to detect small (~10^{-4}) changes in the intensity of the probe. The pump-induced reflectivity change is logged by the difference between the photodiode signal at pump-probe delay t (S_t) and the initial signal (S_0). The step size of the pump-probe time delay is set at 20 femtoseconds. A liquid nitrogen cooled cryostat (SuperTran, Janis) was used in the temperature dependence experiments with temperature control error of < 0.2 K.

Raman spectroscopy. The Raman scattering measurements were carried out on a home-built microscope with a 100×, NA 0.75 objective (Zeiss LD EC Epiplan-Neofluar) in a reflection geometry. A 1064 nm CW laser was first filtered with a volume Bragg grating (VBG) and then focused on the sample (001) surface with power density of 1.9 mW·μm^{-2}. The Raman scattered light was collected and separated from Rayleigh scattering by two ultra-narrowband VBG notch filters. The Raman signal was dispersed by a grating and detected by an InGaAs camera (PyLoN-IR, Princeton Instruments). The Raman shift was calibrated by a silicon substrate. The rotational-anisotropy was obtained by rotating the polarization of the incident beam. The sample was mounted in a cryostat (Montana Instruments Fusion/X-Plane) under a vacuum of <10^{-4} Torr.

Self-interaction error evaluation. Other than the widely used PBE functional, which always leads to the spurious delocalization of the localized charge due to the well-known self-interaction error (SIE), DFT+U and hybrid functionals are often employed in the polaron investigation to alleviate the SIE [1]. Compared to DFT+U, in which U is generally treated as a parameter, hybrid functionals are robust, predictive, transferable and generally yield well-behaved crystal properties. The generalized Koopmans condition [2], a requirement of exact functional, is usually used to evaluate the SIE and the piecewise linearity of the functional used in polaron investigation.

$$-I(N + 1) \equiv E(N + 1) - E(N) = \varepsilon_{N+1}(N + 1) \qquad (1)$$

Here, I(N) and E(N) are the ionization energy and total energy of an N electron system, respectively. $\varepsilon_N(N)$ is the Nth eigenvalue of an N electron system. In an exact functional, the 2nd and 3rd parts in Eq. 1 are equal, while in an approximate functional, the deviation of these two terms usually represents SIE. Using Eq 1, we found the default PBE0 hybrid functional gives a 52 meV SIE, which indicates the default PBE0 functional works fairly well to investigate polaron in Bi_2O_2Se. Considering the transferability, we used the standard PBE0 hybrid functional without any further parametrization.

Polaron optimization. The polaron optimization is carried out with PBE0 hybrid functional [3] using the auxiliary density matrix methods (ADMM) [4] as implemented in CP2K [5]. The polaron geometry is represented with a 4 × 4 × 6 conventional cell, which has 960 atoms with optimized lattice constants (a = b = 15.6 Å and c = 73.5 Å). The polaron geometry is relaxed with an extra electron through spin-polarized calculation. The convergence criterion of force is 1e^{-4} Hartree/Bohr. The core–valence interactions are described through Goedecker–Teter–Hutter (GTH) pseudopotentials and the valence electron wave functions are expanded in a double-ζ valence polarized (DZVP) basis. The van der Waals interactions are considered with rVV10 functional [6]. 1350 Ry and 60 Ry cutoff are used for Planewaves and Gaussians, respectively. The finite-size effects are assessed with 5 × 5 × 6 supercell as shown in Supporting information. Both lattice constants, polaron charge distribution, polaron state energy, and polaron formation energy are well converged with the 4 × 4 × 6 conventional cell.

Ab initio Molecular Dynamics. The non-equilibrium dynamics of coupled electrons and nuclei were simulated by molecular dynamics. The AIMD simulations are carried out with Vienna Ab Initio Simulation Package (VASP) [7–9]. The electron-nuclei interactions were described using the projector augmented-wave method [10]. Considering the computational cost of hybrid functional and huge simulation cell that need to imitate large polaron, the non-local optB88-vdW functional is employed. The energy cutoff for the plane-wave basis sets is set to 520 eV. The simulation is

modeled by a 1 × 1 × 6 supercell of conventional cell. A 4 × 4 × 1 Monkhorst−Pack k-point meshes are used to sample the Brillouin zone. It is noted that although the polaron cannot be optimized using the PBE level functional due to spurious delocalization of charge, the dynamical 2D polaron character can still be simulated by AIMD simulation as the excessive negative charge is sufficiently localized with dynamic disorder in AIMD simulation (Fig. S10).

Additional Data

Temperature-dependent Raman Spectra.
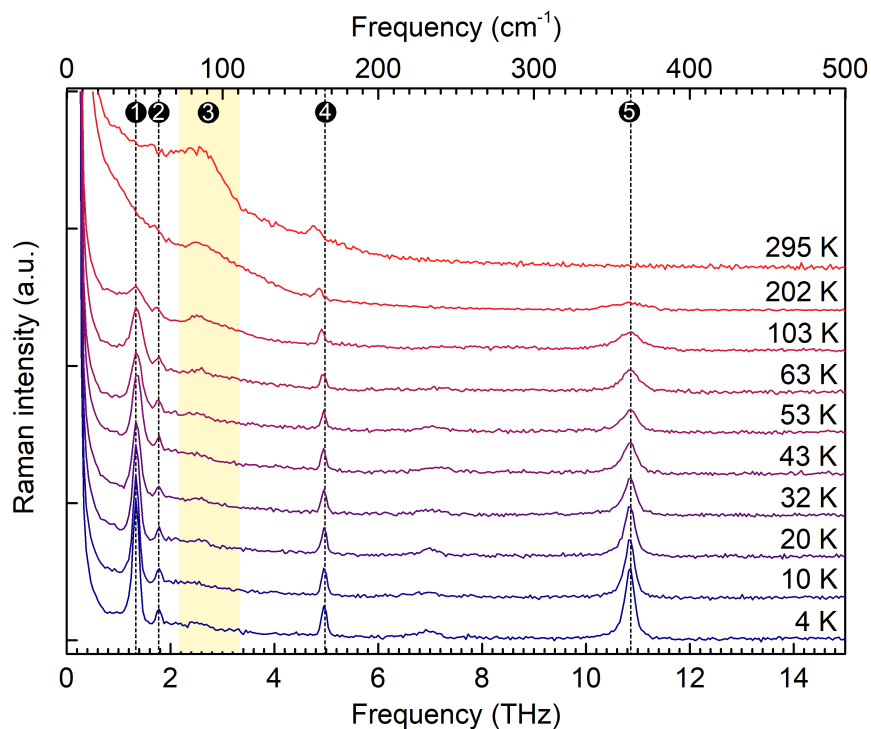
Fig. S1 Temperature-dependent low-frequency Raman spectra of bulk Bi$_2$O$_2$Se single crystals. The diffuse peak extending from zero to ~6 Thz is intrinsically ascribed to the spatial and temporal thermal fluctuations of the structure, implying that Bi$_2$O$_2$Se single crystals show liquid-like lattice anharmonicities. The peaks #1–5 were assigned and summarized in Table S1.

Table S1. Assignment of Phonon Modes in the Low-Frequency Raman Spectra.

Label #	Mode	Frequency (THz)	Frequency (cm^{-1})	Description
1	E_u^*	1.35	45	Bi and Se out-of-phase movement along the layer (shear interlayer mode)[a]
2	A_{2u}^*	1.77–1.65	59–55	Bi and Se out of-phase movement perpendicular to the layer (longitudinal interlayer mode)[a]
3	Broad band	~2.40	~80	Dampled mode likely due to the LO phonon–plasmon coupling[11]
4	A_{1g}	4.95–4.74	165–158	Bi out-of-phase interlayer out-of-plane motion (layer breathing mode)
5	B_{1g}	10.8	361	O out-of-phase intralayer out-of-plane motion

[a]Possible expressions of E_u and A_{2u} IR mode due to symmetry breaking. Similar phenomena were found in layered $MoTe_2$ systems that the inversion symmetry breaking allowed the IR mode (e.g., A_u and B_u symmetries) to be observed in the Raman spectrum[12].

Raman tensor analysis. Bulk Bi_2O_2Se in the ground state belongs to the space group $I4/mmm$. The Bi, O and Se atoms are located at Wyckoff positions of 4e, 4d and 2a, respectively. At the Γ point, the point group is D_{4h}, which contains symmetry elements of E, $2C_4$, C_2, $2C_2'$, $2C_2''$, i, $2S_4$, σ_h, $2\sigma_v$ and $2\sigma_d$. Then the lattice vibration representation is

$$\Gamma = A_{1g}(R) + 2A_{2u}(IR) + B_{1g}(R) + 2E_u(IR) + 2E_g(R) + A_{2u}(Acoustic) + E_u(Acoustic)$$

which indicates that ground-state bulk Bi_2O_2Se has four Raman-active modes, four infrared-active modes and two acoustic modes. The Raman tensors that determine the selection rules are

$$R_{A_{1g}} = \begin{pmatrix} a & 0 & 0 \\ 0 & a & 0 \\ 0 & 0 & b \end{pmatrix} \quad R_{B_{1g}} = \begin{pmatrix} c & 0 & 0 \\ 0 & -c & 0 \\ 0 & 0 & 0 \end{pmatrix} \quad R_{E_g^1} = \begin{pmatrix} 0 & 0 & e \\ 0 & 0 & 0 \\ e & 0 & 0 \end{pmatrix} \quad R_{E_g^2} = \begin{pmatrix} 0 & 0 & 0 \\ 0 & 0 & f \\ 0 & f & 0 \end{pmatrix}$$

The experiments are performed in a backscattering configuration where the incident light is aligned with the normal of the sample, i.e., z-axis, and the angle θ is the angle between the

polarization of the light and the x-axis of the sample. The incident light vector is $\hat{e}_i = (\cos\theta, \sin\theta, 0)$ and the scattering light vector is $\hat{e}_s = (\cos\theta, \sin\theta, 0)$ for parallel-polarized configuration and $\hat{e}_s = (-\sin\theta, \cos\theta, 0)$ for cross-polarized configuration. For $\theta = 0$, the parallel and cross polarization geometries are described by $\overline{Z}(XX)Z$ and $\overline{Z}(XY)Z$, respectively, in the Porto notation. Therefore, the Raman cross-section $S = |\hat{e}_i^* \cdot R \cdot \hat{e}_s|^2$ is
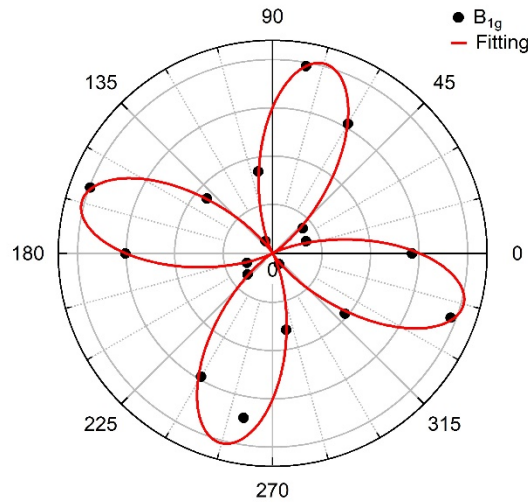
$$S_{A_{1g},\parallel} = a^2, \, S_{A_{1g},\perp} = 0$$

$$S_{B_{1g},\parallel} = \frac{c^2}{2}(\cos 4\theta + 1), S_{B_{1g},\perp} = \frac{c^2}{2}(1 - \cos 4\theta)$$

$$S_{E_g^1,\parallel} = 0, \, S_{E_g^1,\perp} = 0$$

$$S_{E_g^2,\parallel} = 0, \, S_{E_g^2,\perp} = 0$$

We can find that the two E_g modes do not show Raman intensity and only two Raman peaks, A_{1g} at 158~165 cm^{-1} (4.74~4.95 THz) and B_{1g} at 361 cm^{-1} (10.8 THz), can be observed in our experimental geometry. Thus, mode 1 and mode 2 in the spontaneous Raman spectra should not be assigned to the doubly degenerate E_g modes.

Fig. S2 Polarization angle dependence of phonon modes in cross-polarized Raman spectra of Bi$_2$O$_2$Se at 104 K. The polarization dependence of B_{1g} mode follows the Raman selection rule of a D$_{4h}$ point group. The fitting function is $|A(1 - \sin(4\theta + \varphi_0))|$, where A is propotional to the

square of the Raman tensor element, φ_0 is the phase, and θ is the in-plane angle between excitation light and the crystalline axis.

Analysis of coherent phonon spectra
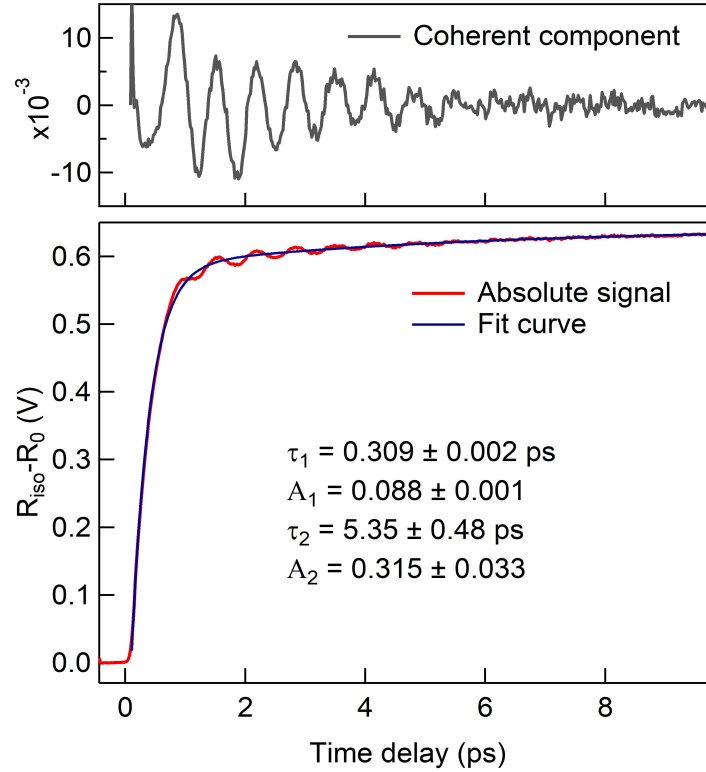
Fig. S3 Extraction of coherent oscillation component from the isotropic transient reflectance. The incoherent response is fitted using a double exponential function convoluted with Gaussian model (blue). The time constants (τ_1 and τ_2) and the corresponding amplitudes (A_1 and A_2) are shown in the inset. The upper panel shows the coherent residue after subtracting the incoherent part. Experiment condition: pump at 2.26 eV, T = 90 K.
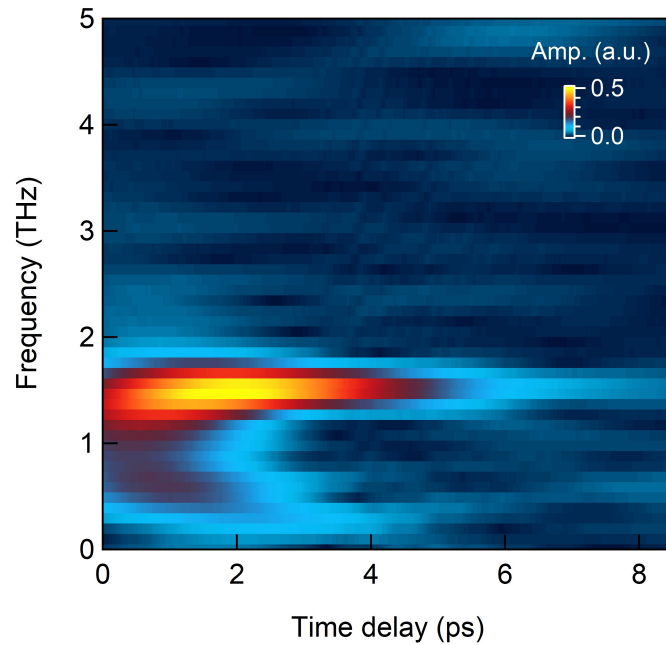
Fig. S4 Short-time Fourier transform (STFT) of the coherent oscillation obtained by subtracting the incoherent part in time-domain data. It shows that the reflectance of the probe pulse is modulated by a single-frequency (~1.515 THz) mode excited by the ultrafast pump pulse. Zero-padding with size of twice of the data points is added in both ends of the data. A window size of 300 is used to apply the STFT.
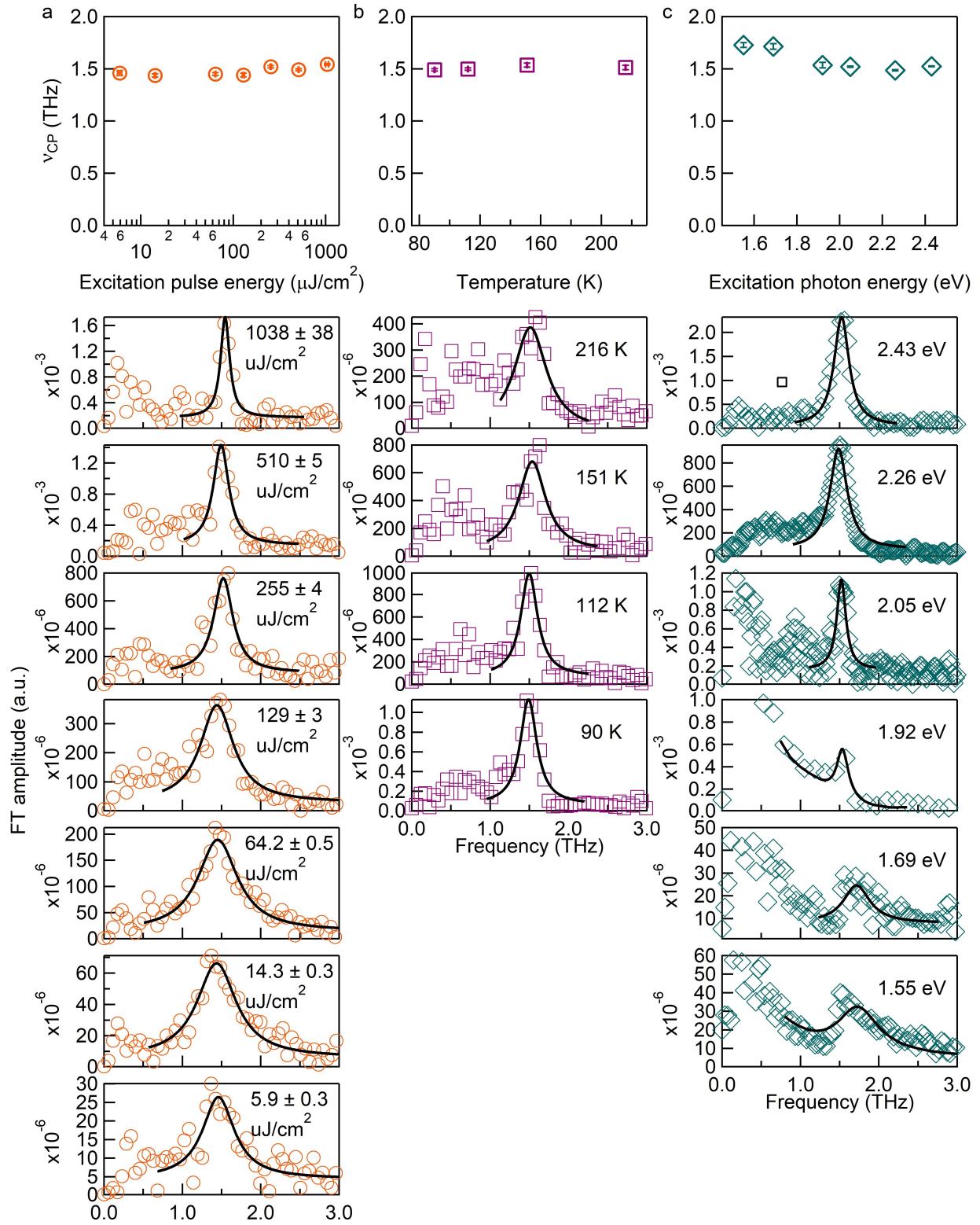
Fig. S5 Coherent phonon frequency (ν_{CP}) and amplitude as a function of excitation pulse energy (a), temperature (b), and excitation photon energy (c), respectively. The

corresponding FT spectra and the Lorentz fittings are shown in the lower panels. (a) A series of pulse energies (5.9 ± 0.3, 14.3 ± 0.3, 64.2 ± 0.5, 129 ± 3, 255 ± 4, 510 ± 5, 1038 ± 38 μJ cm^{-2}) of a 2.26 eV excitation pulse are used. No obvieous electronic softening is observed in the excitation pulse energy dependent measurements. (b) Temperature dependent experiments pumping at 2.26 eV are conducted at 90 K, 112 K, 151 K, 216 K, and 293 K. With increasing the temperature, the system undergoes a faster dephasing resulting in the decrease in both lifetime and amplitude of the coherent lattice vibration. No clear coherent phonon signal is observed at room temperature. The dephasing might be due to the activation of the phonon−phonon scattering in a strongly anharmonic lattice. (c) Excitation photon energy dependent measurements by pumping at 1.55, 1.69, 1.92, 2.05, 2.26, and 2.43 eV. The exponential background in the FT spectra of 1.55, 1.69, 1.92 eV conditions is due to the insufficient incoherent signal subtraction.
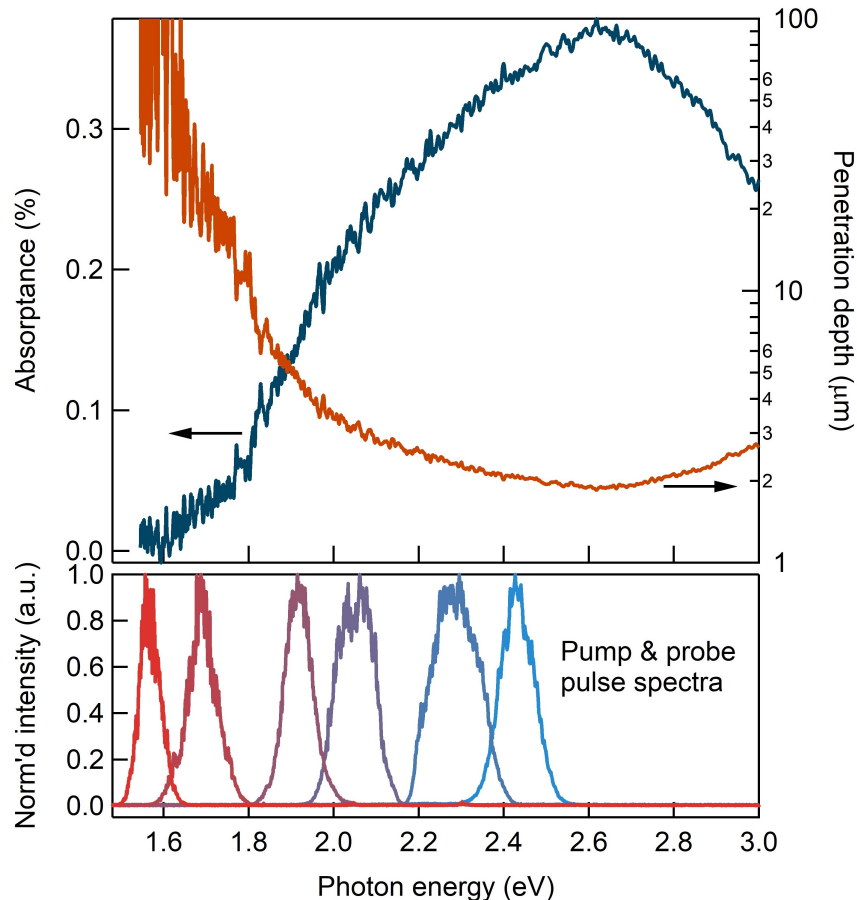
Fig. S6 Absorptance as a function of photon energy of a 7 nm thick Bi₂O₂Se thin layer and the calculated penetration depth. For a layer of material with thickness << λ on a thick transparent substrate, its reflectance contrast is proportional to the absorptance based on the equation of the fractional reflectance change from the Maxwell's equations.[13] Therefore, the absorptance spectrum and the energy-dependent penetration depth can be estimated based on the published work.[14] Here, λ is the wavelength of the visible and near-infrared light and the substrate is a 0.3 mm thick Mica. Since no obvious quantum-size effects show in optical properties of Bi₂O₂Se with layer number larger than 6, the absorptance and penetration depth calculated from the 7 nm thick (11 layers) sample is a good estimation for the bulk crystals used in our experiments. The corresponding penetration depth is calculated for the bulk crystal (orange curve). Lower panel shows the pump and probe pulse profiles used in the coherent phonon spectroscopy. The center energies are 2.43, 2.26, 2.05, 1.92, 1.69, and 1.55 eV. The corresponding pulse durations measured by the frequency-resolved optical grating (FROG) method are 30 ± 3 fs, 30 ± 3 fs, 31 ± 3 fs, 38 ± 3 fs, 33 ± 6 fs, and 45 ± 5 fs. The bandwidth is in the range of 10 to 28 THz.
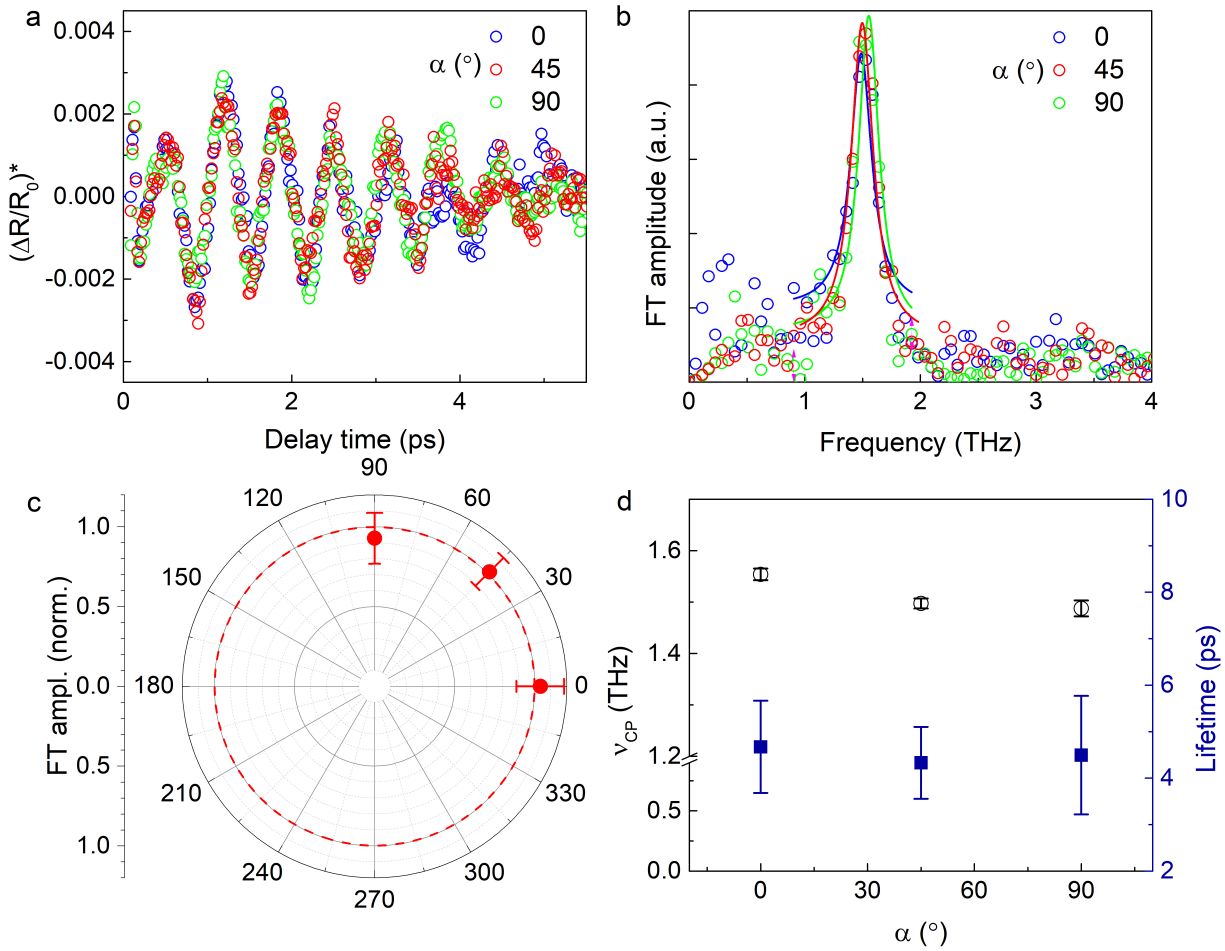
Fig. S7 Pump-probe polarization angle dependence of the coherent phonon. The time-domain (a) and Fourier transform (b) of the oscillatory part of the coherent phonon with subtracting the incoherent background. The measurements are conducted by fixing the angle between probe polarization and an in-plane crystalline axis ($\theta = 0°$) and varying the pump-probe polarization angles ($\alpha = 0°, 45°, 90°$). The incoherent background is obtained by fitting with a Gaussian convoluted with double exponential function. Normalized Fourier-transform amplitude (c) and coherent phonon frequency/lifetime (d) at different α. Within experimental uncertainty, the invariance of CP characteristics as a function of pump-probe polarization angle indicates the isotropic nature of the coherent lattice vibration.
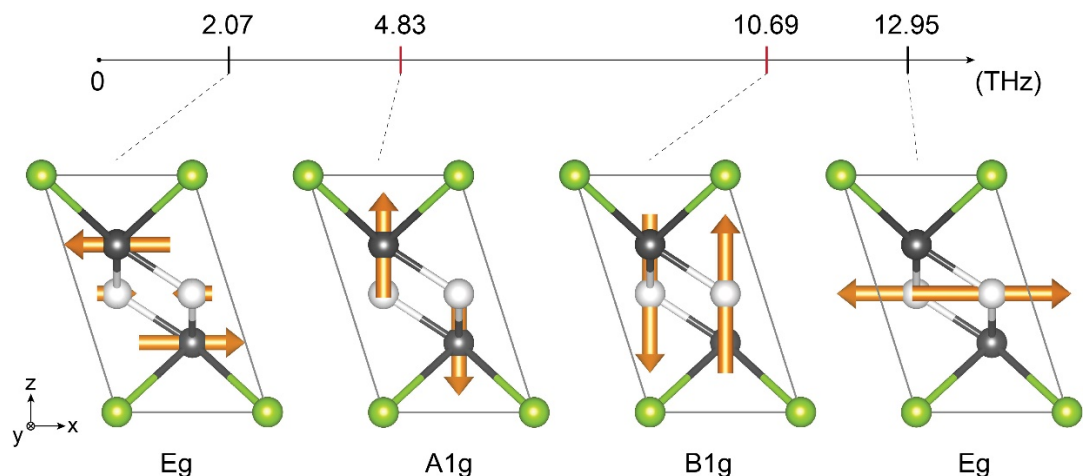
Fig. S8 Eigenfrequency and eigenvector of Raman active modes in *I4/mmm* Bi$_2$O$_2$Se calculated using the combination of VASP[7–9] and Phononpy[15] codes. Primitive cells are shown. Orange arrows indicate the atomic movements. Based on the Raman tensor and the vertical incidence to the (001) surface, only A$_{1g}$ and B$_{1g}$ can be observed (red tick) and no Raman modes with out-of-plane motions are allowed at frequency < 4.8 THz in the harmonic calculations of the ground electronic state. Bi, black; O, white; Se, green.
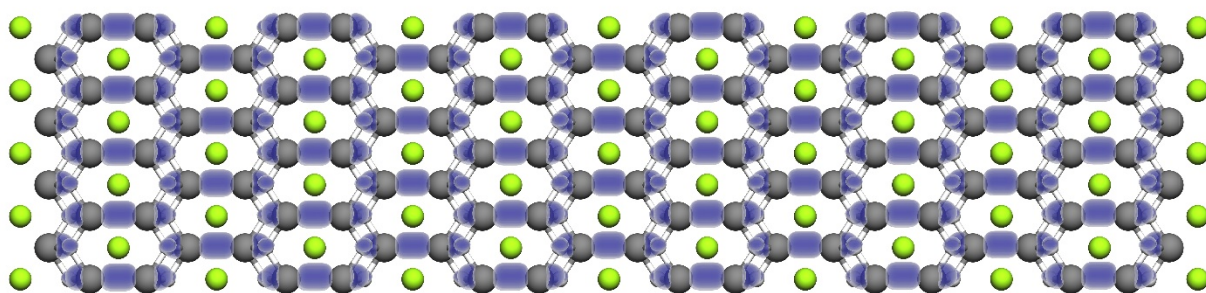
Fig. S9 Charge distribution of CBM of Bi$_2$O$_2$Se^0. The calculation are performed using CP2K with PBE0 hybrid functional. The simulation detatils are same as those used in the simuation of the excesee negative charge distribution of Bi$_2$O$_2$Se^{-1} (Fig. 3a). Bi, black; O, white; Se, green.
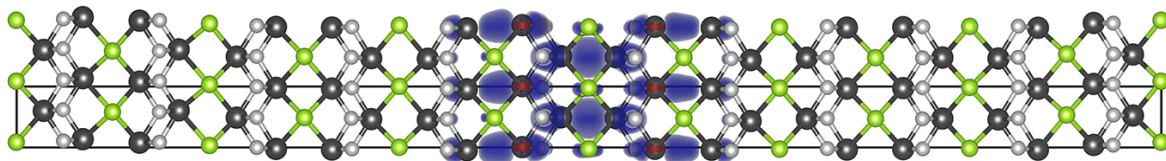
Fig. S10 A representative snapshot of the excess charge distribution in an *ab initio* molecular dynamics (AIMD) trajectory at 50 K for BiSe$_2$O$_2$$^{-1}$. Nonlocal opt88-vdW is used with 1×1×6 supercell. Bi, black; O, white; Se, green. It is noted that although the polaron can not be optimized using the PBE level functional, the dynamical 2D polaron character can still be achieved in AIMD simulation.

Note S1. Hot carrier cooling in Bi$_2$O$_2$Se crystals

Fig. S11 shows the hot carrier cooling with time constants of 0.40 ± 0.07 ps and 0.50 ± 0.05 ps of Bi$_2$O$_2$Se crystals at 112 K and 294K, respectively. The hot carrier lifetime shortens with decreasing *T*. At 112 K, the majority of electrons with excess energies cool down to the conduction band minimum (at Γ point) within 1 ps after photo-excitation.

In a tr-2PPE experiment (detailed elsewhere[17]), the pump laser pulse in the visible regime is generated by a NOPA pumped by the third harmonic of an Yb-doped fiber laser (Clark-MXR, Impulse), and the probe pulse of energy ~5.9 eV is produced by frequency quadrupling the second infrared NOPA pumped by the second harmonic of the same Yb-doped fiber laser. The pulse energy reported in the manuscript are 10 nJ and 10 pJ, respectively, with a repetition rate of 0.82 MHz. The time resolution of the tr-2PPE experiment is ~ 130 fs. The Bi$_2$O$_2$Se sample is mounted on a highly doped Si substrate with native oxide layers by vacuum compatible silver epoxy and the top surface is covered by the same epoxy and a copper post for in situ cleaving. After hours of outgassing at ~150 °C under ultrahigh vacuum (UHV, 10^{-10} mbar), the sample is cleaved under

the same UHV condition for experiment. The sample was biased by an external voltage of -3 V with respect to ground.
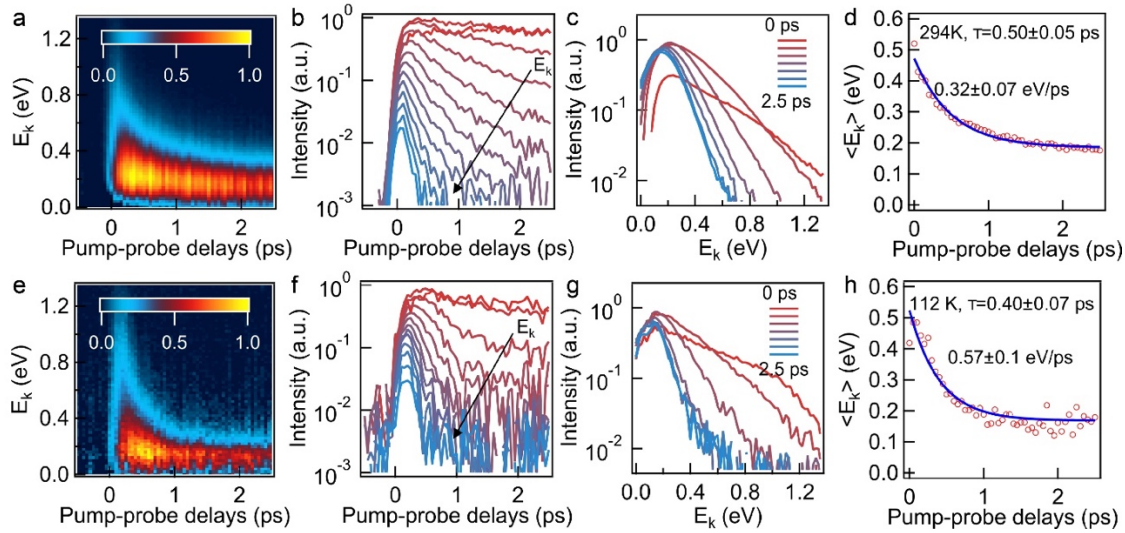
Fig. S11 Time-resolved two-photon photoemission spectra (tr-2PPE) on the (001) surface of Bi$_2$O$_2$Se crystals. (a) Pseudocolor plot of normalized room temperature tr-2PPE spectra as a function of pump-probe delays, for pump and probe energies of 2.25 eV and 5.9 eV, respectively. The pump-induced hot electrons cool down significantly within ~1 ps to near the conduction band minimum (CBM). Color scale indicates normalized photoelectron counts. (b) Hot electron dynamics at selected constant kinetic energies from 0.1 eV (red) to 1.3 eV (blue), showing a transient (< 200 fs) population at the higher energy tail and a pile-up of electrons at the CBM. (c) Energy distribution curves (EDC) for selected time delays. The hot electron quasi-equilibrium is established on ~100 fs time scale as evidenced by the tail of the EDCs, which cool down to CBM within 1 ps. Cuts taken from (0, 0.2, 0.5, 1.0, 1.5, 2.0 and 2.5 ps). (d) Average kinetic energy $\langle E_k \rangle = \int I(E_k)E_k dE_k / \int I(E_k)dE_k$ for the observed hot electron relaxation, with a characteristic lifetime of 0.5 ps. Within 0.5 ps, linear fitting of the cooling rate gives the rate of 0.32 eV/ps. (e-f) The corresponding tr-2PPE spectra, transient hot electron dynamics, EDCs and average kinetic energies when the sample is kept at 112 K. A faster hot electron cooling rate of ~0.57 eV/ps is observed due to the dominating phonon emission which is more favorable at lower T[16]. Therefore, most of the hot carriers cool down to the conduction band minimum at the Γ point within 1 ps at 112 K.

Note S2. Finite-size effect evaluation for polaron formation

The finite-size effect of two-dimension (2D) polaron formed in $Bi_2O_2Se^{-1}$ is evaluated by using 4×4×6 and 5×5×6 supercell. In both cases, all lattice constants and atomic geometry are relaxed with an extra electron using PBE0 hybrid functional. As shown in Table S2, the lattice constants converge for different supercell sizes. The energy gap between CBM and polaron state ($E_{CBM-polaron}$) and polaron formation energy ($E_{formation}$) decrease slightly with the increase of supercell size.
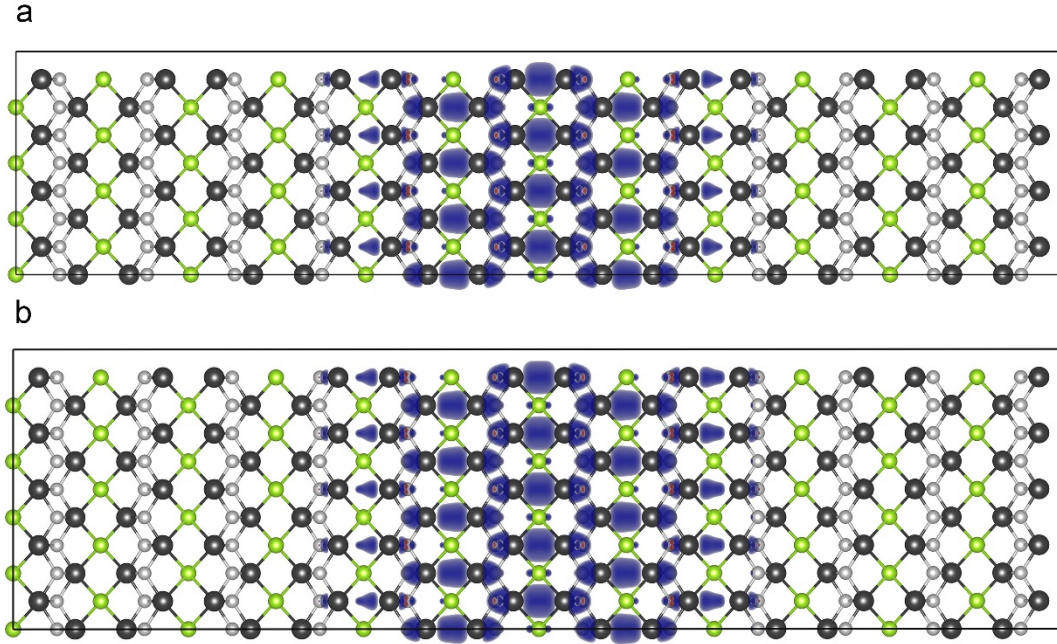
a

b

Fig. S12 Distribution of the excess charge in $Bi_2O_2Se^{-1}$ using 4×4×6 (a) and 5×5×6 (b) supercell. Bi, black; O, white; Se, green.

Tabal S2. The Lattice Constants, $E_{CBM-Polaron}$ and $E_{Formation}$ of $Bi_2O_2Se^{-1}$ Calculated with 4×4×6 and 5×5×6 Supercells.

|	a (Å)	b (Å)	c (Å)	$E_{CBM-Polaron}$ (meV)	$E_{Formation}$ (meV)
4×4×6	3.903	3.903	73.473	146	14.2
5×5×6	3.903	3.903	73.456	141	13.9

Note S3. Rationalizing peaks presented in AIMD
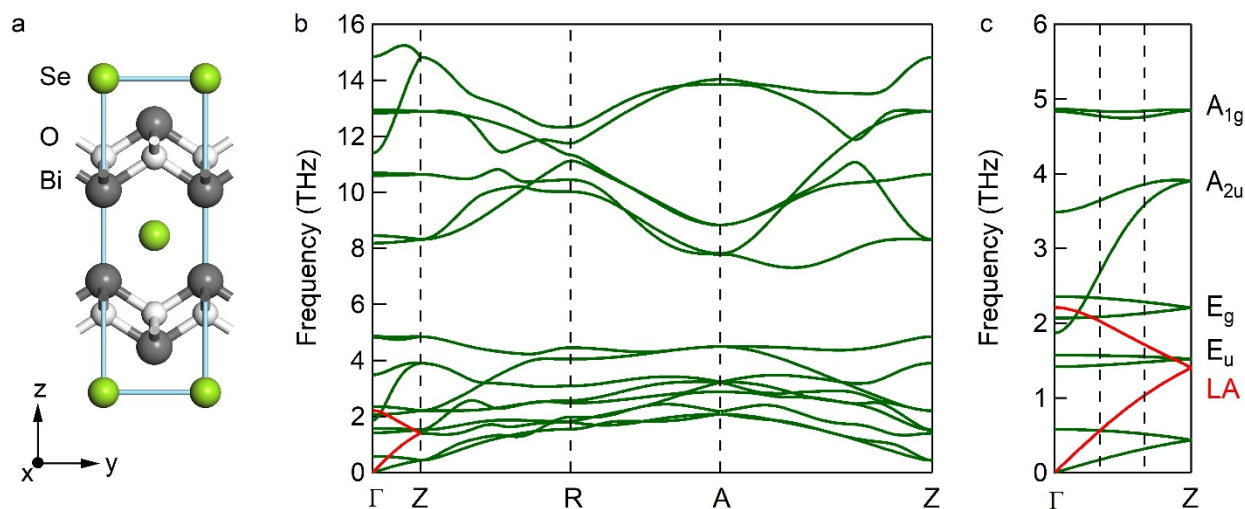
Fig. S13 Phonon dispersion of Bi$_2$O$_2$Se^0. (a) The unit cell of Bi$_2$O$_2$Se^0 that used to calculate the phonon dispersion. (b) Phonon dispersion of Bi$_2$O$_2$Se^0 (c) The phonon dispersion of the unit cell along Γ-Z direction. The dash lines represent the K-points folded into Γ point of the 1×1×6 supercell, which can present in the AIMD simulation. The longitudinal acoustic (LA) phonon mode is marked by red line in (b) and (c). The phonon dispersion is calculated with the combination of VASP [7–9] and Phonopy [15] code.

In this note, we rationalize the peaks presented in Fig.3d. We use the 1×1×6 supercell to perform the molecular dynamics. As indicated in Figure S13c, the substantive phonons along Γ-Z direction in the unit cell will be folded into the gamma point of the supercell. These phonons can present and be FFT-observable if they are excited in the AIMD simulation. Based on the phonon frequencies and phonon polarization vector, we have assigned the phonon peaks in Fig. 3d to the LA modes at different K-points (LA@K*), A$_{2u}$ mode at Γ point and different K-points (A$_{2u}$@Γ and A$_{2u}$@K*), and A$_{1g}$ mode at Γ point and different K-points (A$_{1g}$@Γ and A$_{1g}$@K*).

Note S4. Signature A$_{1g}$ phonon of polaron (Bi$_2$O$_2$Se^{-1})
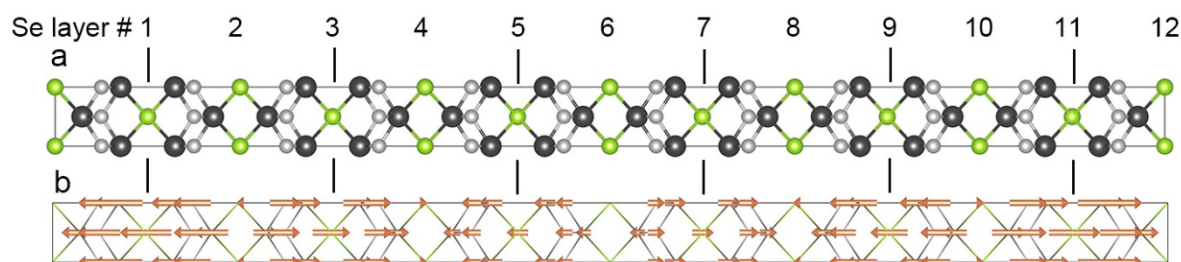
Fig. S14 Signature A$_{1g}$ phonon from normal modes calculation (a) Optimized geometry of polaron in Bi$_2$O$_2$Se^{-1}. The polaron geometry is optimized using CP2K and PBE0 hybrid functional

with a 4×4×6 supercell. Since the lattice distortion is homogeneous along the 2D layer direction, here only a 1×1×6 geometry is shown. The optimized geometry can be imposed by a *P4/mmm* group with all atomic position deviations are less than 0.002 Å. (b) Unprecedented A_{1g} mode after polaron formation calculated using CP2K and Phonopy[15] with PBE0 hybrid functional.

Note S5. Signature A_{1g} phonon of polaron

We performed DFT calculations PBE0 functional on a 2D thin Bi_2O_2Se film with 7 sub-layer and we found the polaron still exists and retains its shape as shown in Fig. R3 (b). Figure R3 (a) shows the density of states (DOS) of 2D Bi_2O_2Se and $Bi_2O_2Se^{-1}$. The polaron state appreas at -0.46 eV below the conduction band minimum (CBM) for $Bi_2O_2Se^{-1}$. The formation energy is calculated to be 39.2 meV. Figure R3 (c) shows differential charge density between the polaron state of $Bi_2O_2Se^{-1}$ and CBM of Bi_2O_2Se, where the red and blue colors indicate the electron depletion and accumulation, respectively. It indicates polaron formation enhances the Bi-Bi bond and repulse the charge localized on Se and O.

It should be noted that we use the hydrogen atoms to saturate the dangling bonds in 2D Bi_2O_2Se. Such a treatment may influence the value of polaron formation energy. In addition, the electron-hole (*e-h*) interaction is not considered in such a calculation. We propose the *e-h* interaction will further stabilize the 2D polaron and a polaron-exciton can be formed. We believe a follow-up to study the formation of polaron-exciton and its coupling with phonons on both theoretical and experimental sides will be really exciting.
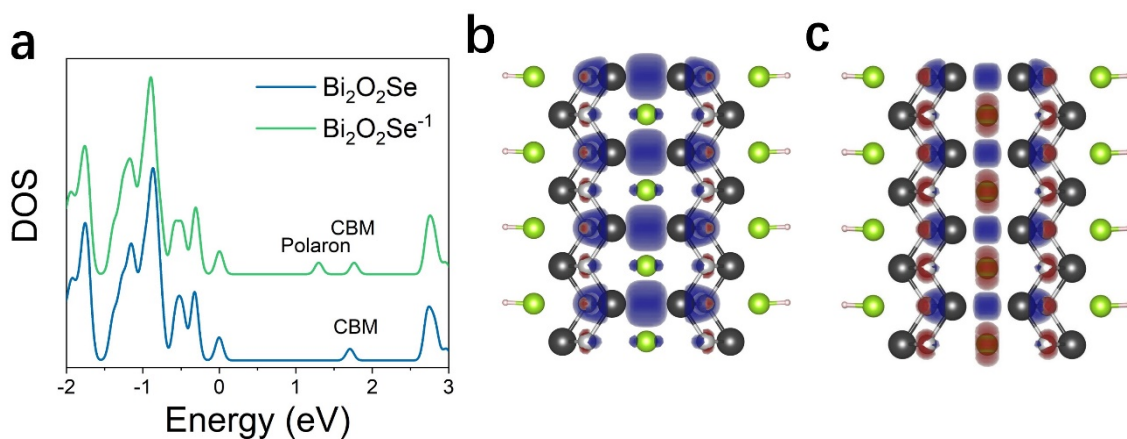
Fig.S15. a, Total DOS at Γ point of the Bi_2O_2Se and $Bi_2O_2Se^{-1}$. The energy references are set to valance band maximum (VBM). b, Excess charge distribution for fewlayers $BiSe_2O_2^{-1}$. Bi,

black; O, white; Se, green, H, pink. It is noted that hydrogen atoms are used to saturate the dangling bonds. c, Differential charge density between polaron state of $Bi_2O_2Se^{-1}$ and CBM of Bi_2O_2Se. The red and blue colors indicate the electron depletion and accumulation, respectively.

Reference

1.   Elmaslmane, A. R., Watkins, M. B. & McKenna, K. P. First-Principles Modeling of Polaron Formation in TiO2 Polymorphs. *J. Chem. Theory Comput.* **14**, 3740–3751 (2018).

2.   Perdew, J. P., Parr, R. G., Levy, M. & Balduz, J. L. Density-Functional Theory for Fractional Particle Number: Derivative Discontinuities of the Energy. *Phys. Rev. Lett.* **49**, 1691–1694 (1982).

3.   Guidon, M., Hutter, J. & VandeVondele, J. Robust Periodic Hartree−Fock Exchange for Large-Scale Simulations Using Gaussian Basis Sets. *J. Chem. Theory Comput.* **5**, 3010–3021 (2009).

4.   Guidon, M., Hutter, J. & VandeVondele, J. Auxiliary Density Matrix Methods for Hartree−Fock Exchange Calculations. *J. Chem. Theory Comput.* **6**, 2348–2364 (2010).

5.   Kühne, T. D. *et al.* CP2K: An electronic structure and molecular dynamics software package - Quickstep: Efficient and accurate electronic structure calculations. *J. Chem. Phys.* **152**, 194103 (2020).

6.   Vydrov, O. A. & Van Voorhis, T. Nonlocal van der Waals density functional: The simpler the better. *J. Chem. Phys.* **133**, 244103 (2010).

7.   Kresse, G. & Hafner, J. Ab initio molecular dynamics for liquid metals. *Phys. Rev. B* **47**, 558–561 (1993).

8.   Kresse, G. & Furthmüller, J. Efficiency of ab-initio total energy calculations for metals and semiconductors using a plane-wave basis set. *Comput. Mater. Sci.* **6**, 15–50 (1996).

9.   Kresse, G. & Furthmüller, J. Efficient iterative schemes for ab initio total-energy calculations using a plane-wave basis set. *Phys. Rev. B* **54**, 11169–11186 (1996).

10. Kresse, G. & Joubert, D. From ultrasoft pseudopotentials to the projector augmented-wave method. *Phys. Rev. B* **59**, 1758–1775 (1999).

11.   Pereira, A. L. J. *et al.* Experimental and Theoretical Study of Bi2O2Se Under Compression. *J. Phys. Chem. C* **122**, 8853–8867 (2018).

12.   Zhang, K. *et al.* Raman signatures of inversion symmetry breaking and structural phase transition in type-II Weyl semimetal MoTe2. *Nat. Commun.* **7**, 13552 (2016).

13.   Mak, K. F. *et al.* Measurement of the optical conductivity of graphene. *Phys. Rev. Lett.* **101**, 196405 (2008).

14.   Wu, J. *et al.* Controlled Synthesis of High-Mobility Atomically Thin Bismuth Oxyselenide Crystals. *Nano Lett.* **17**, 3021–3026 (2017).

15.   Togo, A. & Tanaka, I. First principles phonon calculations in materials science. *Scr. Mater.* **108**, 1–5 (2015).

16.   Tisdale, W. A., Muntwiler, M., Norris, D. J., Aydil, E. S. & Zhu, X.-Y. Electron Dynamics at the ZnO (10$\bar{1}$0) Surface. *J. Phys. Chem. C* **112**, 14682–14692 (2008).

17.   Dai, Y., Ziffer, M. E. & Zhu, X.-Y. Screening of hot electrons in the ferroelectric semiconductor In2Se3. *Phys. Rev. B* **102**, 195201 (2020).